AIP Advances

Spatial and temporal dynamics of a supersonic mixing layer with a blunt base

Cite as: AIP Advances **11**, 085322 (2021); https://doi.org/10.1063/5.0062145
Submitted: 02 July 2021 • Accepted: 29 July 2021 • Published Online: 17 August 2021

Lantian Li (李蓝天) **and** **Hao Li** (李浩)

Spatial and temporal dynamics of a supersonic mixing layer with a blunt base

Cite as: AIP Advances 11, 085322 (2021); doi: 10.1063/5.0062145
Submitted: 2 July 2021 • Accepted: 29 July 2021 •
Published Online: 17 August 2021

View Online Export Citation CrossMark

Lantian Li (李蓝天)[1] and Hao Li (李浩)[2,a)]

AFFILIATIONS

[1] Science and Technology on Scramjet Laboratory, College of Aerospace Science and Engineering, National University of Defense Technology, Changsha, Hunan 410073, People's Republic of China
[2] Institut für Strömungsmechanik und Technische Akustik (ISTA), Technische Universität Berlin, Müller-Breslau-Straße 8, D-10623 Berlin, Germany

[a)] Author to whom correspondence should be addressed: haolee0928@163.com

ABSTRACT

A supersonic mixing layer with a blunt base is of practical significance to engineering. Two flow configurations with splitter thicknesses of 1 mm (TN) and 5 mm (TK) are simulated using large eddy simulation. The cluster-based network model (CNM) projects the supersonic mixing layer into a ten-centroid based low-dimensional dynamical system. The CNM's outputs of TN and TK cases are compared in order to better understand the spatial and temporal physics. The given baseline case (TN) demonstrates a quasi-steady dynamics with a periodic visit between ten centroids. Each cluster occupies a nearly uniform space region and is also populated with equal probability. The CNM identifies ten centroids associated with these two flow regimes observed in the TK case: Kelvin–Helmholtz vortex and vortex pairing. According to the resolved centroids, increasing the thickness of the splitter plate complicates the flow structures and expands the high-dimensional state space. The CNM presents probable state transitions, revealing that the temporal dynamics in the whole field exhibits highly intermittent behaviors, with large shape modifications but small fluctuations in turbulent kinetic energy. In the near-wake field, the reattachment point and shock wave behave similarly that they move downstream and upstream alternatively. The blunt base supersonic mixing layer, in aggregate, increases the turbulent kinetic energy by 20.5%.

I. INTRODUCTION

A mixing layer is a canonical flow observed in many practical engineering issues, such as noise reduction,[1,2] drag reduction,[3] aero-optic effect,[4] and mixing enhancement.[5–7] Over the past few decades, numerous studies on mixing layers have been carried out. Starting with the incompressible regime, the mixing layer has been extensively investigated from the perspectives of velocity and pressure fields,[9] large-scale coherent structures,[10,11] and their merging/pairing in the entrainment process.[12] Subsequently, Bell and Mehta[13] discovered that the incompressible mixing layers are able to maintain the self-similar state with the averaged profiles of the first and second-order flow quantities. Following the deep insights into the incompressible one, research interest in compressible mixing layers was highly encouraged owing to their wide engineering applications. Ortwerth and Shine[11] experimentally confirmed the presence of large-scale structures in the supersonic mixing layer. However, due to the limitations of experimental optical devices, fine structures cannot be captured. Goebel *et al.*[14,15] first discovered the self-similar state in the supersonic mixing layer, which was later confirmed by the following simulations[16] and experiments.[17,18] Bogdanoff[19] first proposed the convective Mach number (Mc) to quantify the compressible effects, and subsequent researchers have continued to recognize it. Apart from the heat release,[20,21] increasing Mc reduces the expansion of the compressible mixing layer.[15,22] These studies, like the ones mentioned above, are mostly concerned with flow visualization and statistical analysis of flow quantities, with minimal emphasis on dynamics.

The military value of hypersonic aircraft has recently attracted much attention. The development of combined cycle engines is critical as they are the most promising propulsion system for the single-stage-to-orbit air-breathing launch vehicle and the reusable recce/strike airplane platform.[23] The engineering development of combined cycle engines has reignited the research interest in the fundamental studies[24–27] and mixing enhancement techniques[28,29] in the supersonic mixing layer. However, the splitter plate with a relatively thin trailing edge is generally included in the experiments[30–32] for the study convenience, especially in the supersonic regimes since the flow structures are pure at this moment. The velocity inlet in simulations is assigned as a tanh-type profile without taking into account a splitter plate.[24–26] These methods are appropriate to concentrate on the core issues of interest, i.e., a simple mixing layer, nevertheless, disjoint from the engineering practice. In a combined cycle engine, the fuel supply and protective cooling system are imperative constituent parts, which incur the inevitable increase in the thickness of the splitter plate. Thus, the supersonic mixing layer with a blunt base deserves deep exploration.

Some pioneers have illustrated the characteristics of the supersonic mixing layer downstream a splitter plate via experimental means[33] and numerical methods.[34,35] Flow structures and statistic analysis are frequently entailed, but dynamical analysis is rarely concerned. The nonlinear nature in the dynamical system and a large amount of data from both experiments and numerical simulations pose great challenges to understanding the dynamics. The reduced-order model (ROM) is a key enabler for physical understanding. Laizet *et al.*[35] simulated incompressible mixing layers having various geometries of thick splitters by means of direct numerical simulation. The influence of the trailing edge shape is carefully considered on the spatial development of the mixing layer. In addition, the proper orthogonal decomposition (POD) is employed to understand the transition from the wake to the mixing layer. Low-dimensional models were also built using POD to understand the temporal and spatial evolution of the mixing layer.[36,37] However, the POD is conducted by solving the eigenvalue problem on the correlation matrix of any two fields. It tends to mix the temporal and spatial frequencies. The POD modes are closely associated with the eigenvectors instead of the practical physics, which are hard to be interpreted. Dynamic mode decomposition (DMD) is an exciting tool to overcome these drawbacks. Song *et al.*[38] conducted DMD analysis to explore the sound generation mechanisms in mixing layers. DMD successfully captures both the far-field acoustics and the near-field dynamics with a few modes. Soni and De[39] executed DMD to segregate the coherent structures on the basis of the pure frequency in the supersonic mixing layer. The dominant modes capture the breakdown, pairing/merging, and stretching of vortices to aid in understanding the contribution to supersonic mixing. However, DMD modes cannot be ranked according to their importance for flow physics. Due to the linearization of the governing equations in the algorithms,[40] the DMD generally shows weak robustness to the nonlinear dynamics with complicated dynamics, especially with highly intermittent dynamics.[41] Given the success and drawbacks of standard DMD, a few variants of DMD have been proposed, such as recursive DMD,[42] spatial–temporal DMD,[43,44] and optimized DMD,[45] just to name a few.

Most drawbacks mentioned in the POD and DMD can be avoided by means of the cluster-based reduced-order model (CROM). Burkardt *et al.*[46,47] first introduced an approach of centroidal Voronoi tessellation (CVT) to produce a ROM of the Navier–Stokes equation. Subsequently, Kaiser *et al.*[48] proposed a cluster-based Markov model (CMM) that integrates the cluster analysis with a Markov model to identify the transitions between different spatial modes. Then, the CMM is employed to analyze the wake of a high-speed train,[49] twisted cylinder flow,[50] supersonic mixing layer,[51] and turbine wake.[52] Shahbazi and Esfahanian[53] built a ROM using cluster analysis and orthogonal cluster analysis to analyze the lead-acid battery, which continuously enriched the family member of the CROM. In the CMM, the clustering is employed to coarse-grain the data into representative states, and the temporal evolution is modeled as a probabilistic Markov model. In this model, the state vector of cluster probabilities converges to a fixed value representing the post-transient attractor, which leads to the disappearance of the dynamics. To surmount the drawback of the CMM in modeling dynamic evolution, we proposed a cluster-based network model (CNM) in Refs. 54 and 55, which is a universal method for data-driven modeling of nonlinear dynamics from time-resolved snapshots without any prior knowledge. The CNM, a branch of CROM, combines a cluster analysis of an ensemble observations from simulations or experiments and a network model for transitions between the different flow characteristics educed from the cluster analysis. The snapshots are coarse-grained into a small number of clusters with the representative states called centroids. The dynamics is described by a network model with "constant velocity flights" between the centroids.

This study seeks to understand the flow dynamics of a blunt base supersonic mixing layer using the CNM instead of the statistical analysis. Considering various configurations and influence factors in this kind of flow, this paper is studied based on two given examples. This paper is organized as follows: Sec. II briefly describes the physical flow model and large eddy simulation method. The grid independence analysis and code verification are carefully carried out to ensure the accuracy of numerical results. Section III introduces the algorithm of the cluster-based network model step by step, including the pre- and post-processing for the clustering results as well as the method for creating a network model based on them. To give readers an overall expression, the fundamental flow features are briefly described in Sec. IV A. Section IV B compares the CNM results from the two cases in order to provide an in-depth insight into the blunt base supersonic mixing layer. Finally, Sec. V summarizes some key findings.

II. NUMERICAL SIMULATION SETUP

A. Physical model

The physical model in the present simulation is the supersonic mixing layer downstream a splitter plate. We include the splitter plate in the computational domain to reproduce realistic situation as in our previous experiment.[57] Dual parallel streams encounter in the trailing edge of the splitter plate. Interactions happen and gradually generate a mixing layer whose visualization thickness increases along with the streamwise orientation. Figure 1 illustrates the two-dimensional numerical sketch. The flow is described in a Cartesian coordinate where the origin is located in the geometrical center of the starting edge of the splitter plate. The x axis is aligned with the streamwise direction and y axis with the transverse direction. U, P, and T represent the inlet velocity, static pressure, and static temperature, respectively. The subscripts "1" and "2" denote the upper and lower streams, respectively. In this study, two splitter

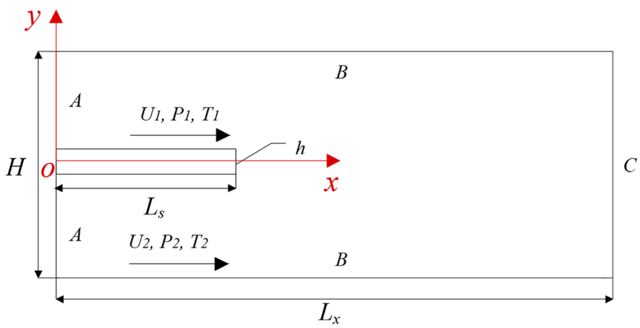

FIG. 1. The two-dimensional sketch of the numerical simulation setup. The numerical domain is rectangular with the dimension excluding a splitter plate. The letters "A," "B," and "C" are used to denote the different boundaries. Two-dimensional simulation is acceptable at $Mc = 0.22$.

plates are considered in the numerical simulations: the thin splitter plate ("denoted by TN") and thick splitter plate (denoted by "TK"). Note that only two-dimensional simulations are conducted since the two-dimensional vortex structures that originated from the Kelvin–Helmholtz (K–H) instability play the absolutely dominant role in the weakly compressible regime with $Mc < 0.4$.[25,56] The mass transfer and combustion in the mixing layer are not involved in this simulation. The two splitter plates (TN and TK) have the same dimension in the length $L_s = 80$ mm but different thicknesses: $h_{TN} = 1$ mm and $h_{TK} = 5$ mm. The convective Mach number is expressed by

$$Mc = \frac{u_1 - u_2}{a_1 + a_2} \tag{1}$$

with the corresponding convective velocity

$$U_c = \frac{U_1 a_2 + U_2 a_1}{a_1 + a_2}. \tag{2}$$

Note that a is the local Mach number. The convective velocity U_c is the averaged moving downstream velocity of the characteristic flow structures. The Reynolds number is based on the convective velocity U_c and thickness of the splitter plate h. They read $Re_{TN} = 3.46 \times 10^4$ and $Re_{TK} = 1.73 \times 10^5$. The computational domain extends a rectangular area excluding the splitter plate,

$$\Omega = L_x \times H - L_s \times h. \tag{3}$$

Many previous literature studies have demonstrated that the splitter plate is of great significance to the vortex dynamics of the mixing layer.[33–35] Herein, we stress the differences between this study and other numerical simulations of the supersonic mixing layers. A tanh-type velocity profile is generally employed as the inlet condition for a rectangular domain. This estimation is convenient for the fundamental analysis on the mixing layer vortex but stay away from the engineering practice.

The dimensions of the computational domain and flow parameters in this numerical study are inspired from our previous numerical[6,7] and experimental study.[57] Notably, the TK case is the same as our experimental study in the supersonic wind tunnel.[6] The TN case is benchmarked as a baseline. The parameters of dual streams are thoroughly listed in Table I.

TABLE I. The parameters of dual incoming streams for numerical simulation.

	Upper		Lower
Convective Mach number Mc		0.22	
Mach number a_1, a_2	2.12		3.18
Convective velocity U_c (m/s)		576.9	
Density ρ (kg/m^3)	0.0556		0.0834
Density ratio $s = \rho_2/\rho_1$		1.5	
Velocity ratio $r = U_2/U_1$		1.2	
Streamwise velocity U (m/s)	519		623
Static pressure P_s (Pa)	2 640		2 520
Total pressure P_0 (Pa)	21 360		101 325
Boundary layer thickness δ (mm)	0.5		0.5

We have to state that many vital variables will affect the supersonic mixing layer's evolution in the downstream. These variables include the thickness and geometrical shape of the splitter plate, the thickness of the initial boundary layer, the Reynolds number, and the convective Mach number. This paper does not discuss these variables and focuses on the dynamics using the cluster-based network model introduced in Sec. III.

B. Numerical method

In our present simulation, the compressible mixing layer is computed using an in-house large eddy simulation (LES) solver based on the finite volume method (FVM). In this solver, the message passing interface (MPI) based on parallel architecture using domain decomposition and distributed memory is employed to gain high calculation efficiency. This solver has been successfully applied to the simulations of the supersonic mixing layer and cavity flow.[6,7,51]

The two-dimensional Navier–Stokes equations are filtered using the Deardorff box filtering[58] and resulting equations are as follows:

Continuity equation,

$$\frac{\partial \bar{\rho}}{\partial t} + \frac{\partial}{\partial x_j}(\bar{\rho}\tilde{u}_j) = 0. \tag{4}$$

Momentum equation,

$$\frac{\partial}{\partial t}(\bar{\rho}\tilde{u}_i) + \frac{\partial}{\partial x_j}\left(\bar{\rho}\tilde{u}_i\tilde{u}_j + \bar{p}\delta_{ij} - \tilde{\tau}_{ij} + \tau_{ij}^{sgs}\right) = 0. \tag{5}$$

Energy equation,

$$\frac{\partial}{\partial t}(\bar{\rho}\tilde{E}) + \frac{\partial}{\partial x_j}\left[(\bar{\rho}\tilde{E} + \bar{p})\tilde{u}_j + \tilde{q}_j - \tilde{u}_i\tilde{\tau}_{ij} + H_j^{sgs} + \sigma_j^{sgs}\right] = 0. \tag{6}$$

Here, ρ denotes the density. $u_i(i = 1,2)$ is the velocity vector in Cartesian coordinates and p is the pressure. The total energy of the system is the sum of the internal energy and kinetic energy. Then, the filtered total energy is determined by the sum of the filtered internal energy, the resolved kinetic energy, and the subgrid kinetic energy. The subgrid-scale stress resulting from the filtering operations is modeled by the subgrid-scale turbulences based on the Boussinesq hypothesis[59] and can be computed by

$$\tau_{ij}^{sgs} - \frac{1}{3}\tau_{kk}\delta_{ij} = -2\mu_t \bar{S}_{ij}, \tag{7}$$

where μ_t is the subgrid-scale turbulent viscosity. The $\bar{S}_{ij}$ is the rate-of-strain tensor for the resolved scale defined by

$$\bar{S}_{ij} = \frac{1}{2}\left(\frac{\partial \bar{u}_i}{\partial x_j} + \frac{\partial \bar{u}_j}{\partial x_i}\right). \tag{8}$$

Note that the isotropic part of the subgrid-scale stress τ_{kk} is added to the filtered pressure term. The compressible form of the subgrid stress tensor is defined as

$$\tau_{ij}^{sgs} = \bar{\rho} u_i \tilde{u}_j - \bar{\rho}\tilde{u}_i\tilde{u}_j. \tag{9}$$

The term can be split into its isotropic and deviatoric parts,

$$\tau_{ij}^{sgs} = \underbrace{\tau_{ij}^{sgs} - \frac{1}{3}\tau_{kk}\delta_{ij}}_{\text{deviatoric}} + \underbrace{\frac{1}{3}\tau_{kk}\delta_{ij}}_{\text{isotropic}}. \tag{10}$$

The deviatoric part of the subgrid-scale stress tensor is modeled using the compressible form of the Smagorinsky model,[60]

$$\tau_{ij}^{sgs} - \frac{1}{3}\tau_{kk}\delta_{ij} = -2\mu_t\left(S_{ij} - \frac{1}{3}S_{kk}\delta_{ij}\right), \tag{11}$$

where the SGS eddy viscosity is

$$\mu_t = \rho L_S^2 |\bar{S}|. \tag{12}$$

In the above equation,

$$|\bar{S}| \equiv \sqrt{2\bar{S}_{ij}\bar{S}_{ij}}. \tag{13}$$

The mixing length for subgrid scales L_s reads

$$L_s = \min(\kappa d, C_s \Delta). \tag{14}$$

In Eq. (14), κ is Karman's constant, d is the distance to the closest wall, and C_s is the Smagorinsky constant. Δ is the scale of the local grid scale and can be computed according to the volume of the computational cell using

$$\Delta = V^{1/3}, \tag{15}$$

and $|\bar{S}|$ is the modulus of rate-of-strain for the resolved scales. Following Ref. 6, C_s is set as 0.1 for the reliable results, which is also found to yield the best results for a wide range of turbulence.

The time-marching is performed by means of a second-order, implicit dual time step scheme to improve the calculating efficiency. A Lower-Upper Symmetric Gauss–Seidel (LU-SGS) method is employed to achieve the inner product. The gradients are calculated by the Green–Gauss cell-based method. The second-order spatially accurate upwind scheme with the low-diffusion Roe Flux Difference Splitting (low Roe-FDS) formulation is utilized in this solver to reduce the dissipation during calculations, which is an updated version of the Roe-FDS. The time step is fixed at $\Delta t = 5 \times 10^{-8}$ s to facilitate the clustering snapshots at convenience. The Courant–Friedrichs–Lewy (CFL) number is less than 0.5. Note that the physical time step Δt is limited only by the level of desired temporal accuracy. The pseudo-time step $\Delta\tau$ in the dual time step scheme is determined by the CFL condition of the implicit time-marching scheme. The calculation case in this paper simulates nearly 2×10^5 time steps to ensure accuracy of the statistical results.

To simulate the actual situation of the boundary layer, the velocity conditions of two inlets with a Blasius flat-plate boundary layer spanning the inlet were determined. The two inlets (denoted by "A" in Fig. 1) are tested by imposing random noise on a mean. The mean profile has a 1/7th power law implemented, and a turbulent kinetic energy of 0.4% is employed. The non-slip boundary and constant temperature conditions (denoted by "B" in Fig. 1) are adopted in the boundaries of the upper wall, bottom sidewall, and splitter plate. The outflow condition (denoted by "C" in Fig. 1) is set as the non-reflective condition[61] for calculation stability. The reflection waves from the outflow boundary are well controlled.

The supersonic mixing layer with the weak compressibility effect ($Mc \leq 0.4$, $Mc = 0.22$ in this paper) will mainly exhibit two-dimensional vortex structures.[8] In addition, the mixing layer with these conditions will exhibit three-dimensional behaviors in a 3D view, but the two-dimensional vortex tubes play the dominant role. Readers are referred to our published results with nearly the same conditions in Ref. 7.

C. Grid independence analysis and code verification

To ensure the simulation's validity and reliability, the grid independence analysis is conducted using three distinct grid systems, namely, coarse, moderate, and refined grids. Table II contains the detailed grid information, including the minimum scale of Δx and Δy required to satisfy the constraints of $x^+ \leq 1$ and $y^+ \leq 1$. The calculation area is discretized into a structured non-uniform grid.

By comparing the statistical profiles at the same spatial position, the effect of grid scales on the numerical results is investigated. As illustrated in Fig. 2, the dimensionless time-averaged temperature and pressure for the TK case at $x/H = 3$ are compared using coarse, moderate, and fine grids, respectively. Three curves for both quantities basically coincide, indicating that no obvious difference exists between numerical results from three grid scales. Additionally, the results from moderate and refined

TABLE II. Three sets of meshes for the 2D numerical simulation of the supersonic mixing layer.

Grid	Coarse	Moderate	Refined
$n_x \times n_y$	838×260	1001×301	1201×351
Cell number	193 980	272 301	375 361
$\Delta y_{\min}$ (m)	2.00×10^{-5}	1.00×10^{-5}	1.00×10^{-5}
$\Delta y_{\max}$ (m)	5.00×10^{-4}	5.00×10^{-4}	5.00×10^{-4}
$\Delta x_{\min}$ (m)	2.00×10^{-5}	1.00×10^{-5}	1.00×10^{-5}
$\Delta x_{\max}$ (m)	5.00×10^{-4}	5.00×10^{-4}	2.00×10^{-4}

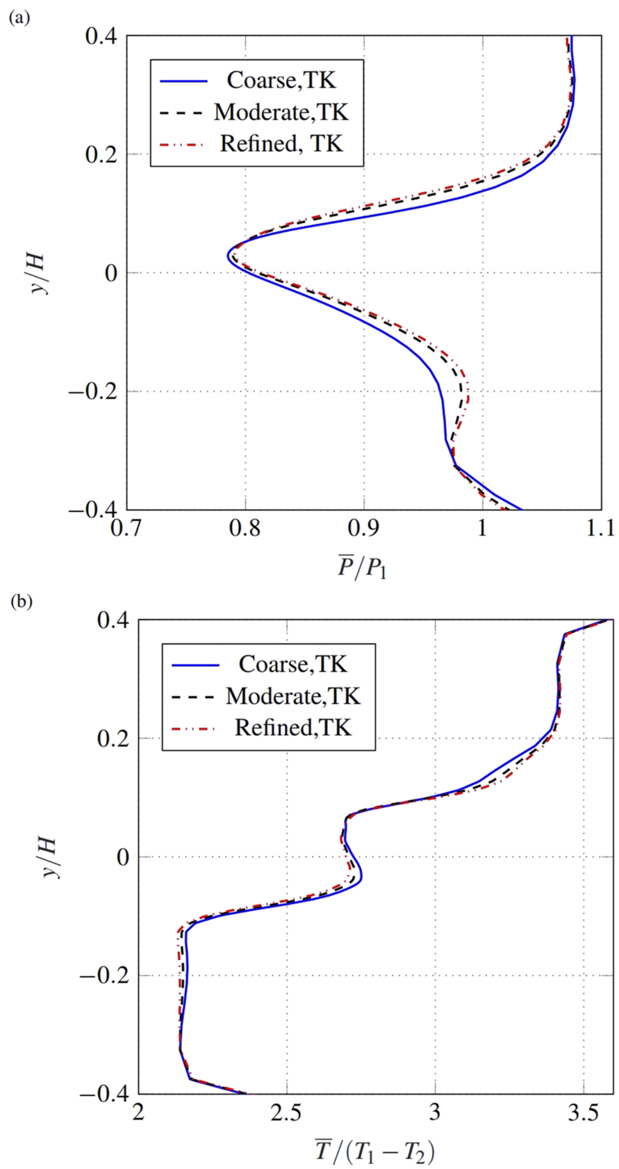

FIG. 2. Comparison of time-averaged profiles in three grid systems at $x/H = 3$ for the TK case. (a) Time-averaged static pressure and (b) time-averaged static temperature.

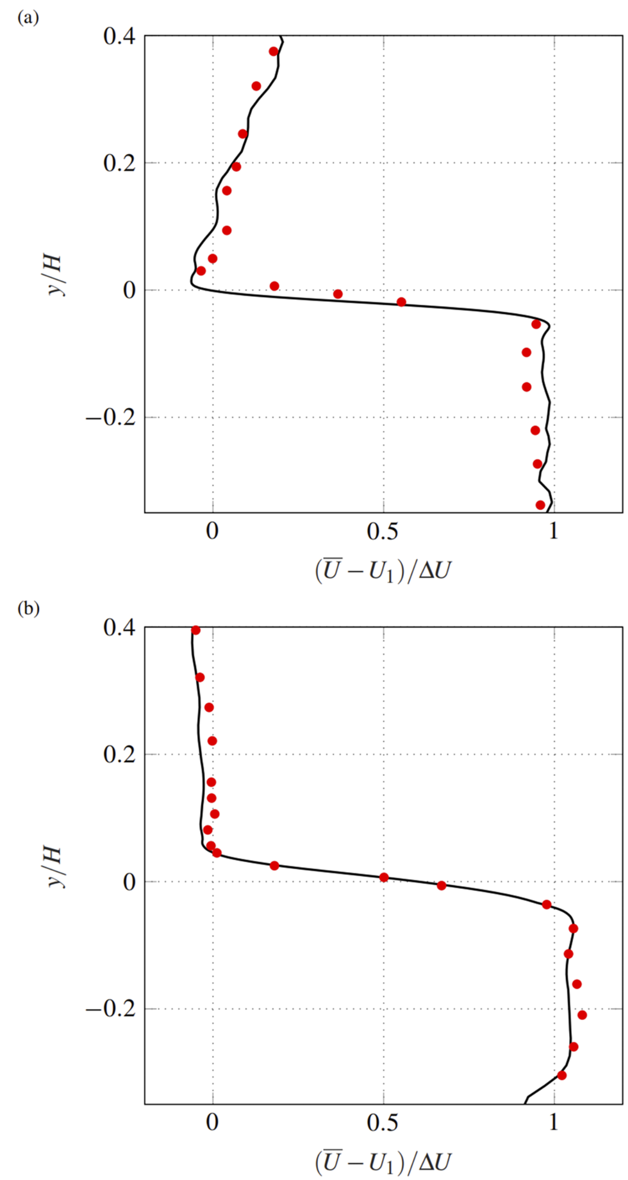

FIG. 3. Streamwise velocity profiles obtained from the numerical results (black solid line) and experimental data (red dots) at (a) $x/H = 2.5$ and (b) $x/H = 3.5$ for the TK case.

meshes are highly comparable. As a result, selecting a moderate grid scale for the computational grid can result in cost and time savings.

We conduct code verification to ensure the solver's reliability. As shown in Fig. 3, the statistical results obtained using the LES solver for the TK case agree reasonably well with the experimental data. *Nota bene*, the experimental data are taken from Ref. 6.

In summary, this LES solver performs admirably well when used to simulate the supersonic mixing layer numerically.

III. CLUSTER-BASED NETWORK MODEL

The cluster-based network model paves a new avenue to model the high-dimensional nonlinear dynamics in a data-driven manner. Figure 4 shows the technical sketch of the cluster-based network model exemplified by the incompressible mixing layer. Cluster analysis groups the high-dimensional state space into a given number of subspaces with the representative states called centroids in an unsupervised manner. Obviously, cluster analysis is indeed one of the dimension reduction techniques. Then, the dynamics is reproduced by the CNM on a directed network, where the nodes are the

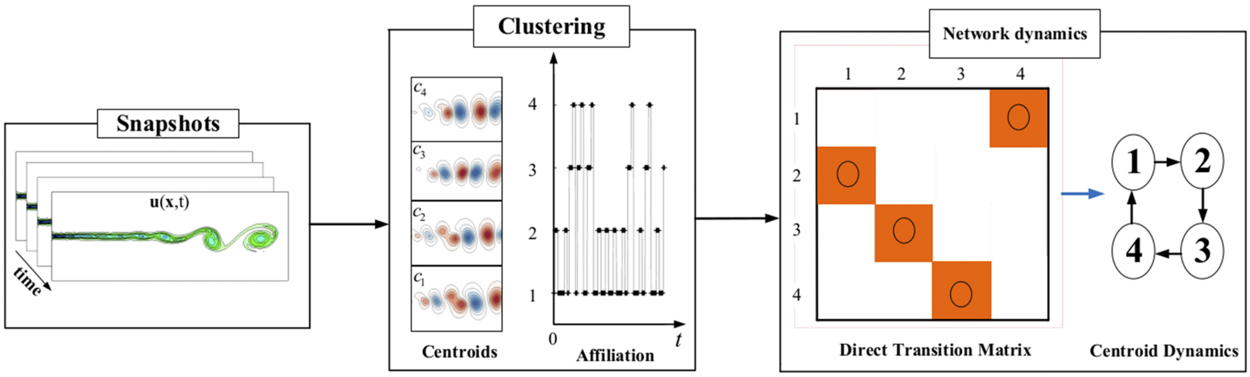

FIG. 4. The methodology sketch of the cluster-based network model. The snapshots $\boldsymbol{u}(\boldsymbol{x}, t)$ are collected at constant sampling frequency. These snapshots are grouped into K clusters in terms of their similarity meanwhile obtaining centroids $\boldsymbol{c}_k$ and cluster affiliations. The representative states, i.e., centroids, are considered as the network nodes. The direct transition probabilities between network nodes are identified from the training data, which describe all possible transitions from the probabilistic point of view. Finally, the complicated dynamics in the high-dimensional state space is converted into a simple dynamics between centroids.

centroids, i.e., the representative states for the subspaces of the system. The transition probability and transition time between nodes can be inferred from the original data. Generally, there are three steps for the CNM analyzing a dynamical system. The data should be collected at first. These data will be coarse-grained into a given number of clusters to get the centroids and time series of labels for each observation. The network is built temporally by means of the time series of labels and spatially by means of the centroids. Network science becomes increasingly popular in nearly all fields of mathematical modeling, including computer sciences, biology, and fluid dynamics.[62–64]

A. Data collection

The CNM is a purely data-driven model to resolve a dynamic system without any prior knowledge. The starting point of the CNM is the data collection of M time-discrete N-dimensional state of the system. Theoretically, any variables can be fed into the CNM due to the great robustness to the nonlinear system. Recommended by the model developers, the interested variables, especially reflecting the property of a dynamic system, should be first picked up. The state represented by the collected data can comprise the full state, the low-dimensional representation of the full state, or an observation. Note that these data can be from the numerical simulations or experiments. In addition, the model quality is directly related to its training data. In particular, the sampling frequency for snapshots must be selected that the relevant dynamics are resolved. The total time range covering these snapshots should ensure the statistic convergence of the dynamics. Therefore, the CNM needs a larger amount of training data than other data-driven models like DMD. In the present study, we collect M time-resolved velocity snapshots in a steady domain Ω as the observation for the CNM. These snapshots are obtained from the numerical simulation described in Sec. II. The velocity field is collected at an instant time step Δt^c and denoted as $\boldsymbol{u}^m(\boldsymbol{x}) := \boldsymbol{u}(\boldsymbol{x}, t^m), m = 1, \ldots, M$. The time step Δt^c should be short enough to capture the characteristic flow features. We emphasize the difference between Δt in LES and Δt^c that two variables should satisfy the requirement of $\Delta t \leq \Delta t^c$.

B. Cluster analysis

1. Data preprocessing: Compression using POD

We consider the POD method as a data compression tool to reduce the computational loads, but this step is not mandatory for the CNM. The data compression is highly recommended for the clustering of large high-dimensional datasets since it is pretty expensive. Lumley[65] first introduced POD into the turbulence community. This method aims to find optimal basis functions by maximizing the mean square projection of the system using a spatial two-point correlation in an eigenvalue problem. The inner product of two square-integrable velocity fields $\boldsymbol{u}_1$ and $\boldsymbol{u}_2 \in L^2(\Omega)$ is given as

$$(\boldsymbol{u}_1, \boldsymbol{u}_2)_\Omega := \int_\Omega \boldsymbol{u}_1(\boldsymbol{x}) \cdot \boldsymbol{u}_2(\boldsymbol{x}) \mathrm{d}\boldsymbol{x}. \tag{16}$$

The corresponding norm reads $\|\boldsymbol{u}\|_\Omega := \sqrt{(\boldsymbol{u}, \boldsymbol{u})_\Omega}$. All collected snapshots are averaged in time to get the mean flow $\boldsymbol{u}_m$. The snapshot-based POD is applied to the velocity fluctuations,

$$\boldsymbol{v}^m(\boldsymbol{x}) = \boldsymbol{u}(\boldsymbol{x}, t^m) - \boldsymbol{u}_m(\boldsymbol{x}). \tag{17}$$

The two-point correlation matrix $\boldsymbol{C} = (C^{mn}) \in \mathbb{R}^{M\times M}$ of the fluctuations is first determined,

$$C^{mn} = \frac{1}{M}(\boldsymbol{v}^m, \boldsymbol{v}^n)_\Omega. \tag{18}$$

The eigenvalue problem for the correlation matrix $\boldsymbol{C}$ is solved to determine the POD modes and time coefficients (i.e., mode amplitudes),

$$\boldsymbol{C}\boldsymbol{e}_i = \lambda_i \boldsymbol{e}_i, \quad i = 1, \ldots, M. \tag{19}$$

Each POD mode is a linear combination of the snapshot fluctuations,

$$\boldsymbol{u}_i = \frac{1}{\sqrt{M\lambda_i}} \sum_{m=1}^{M} e_i^m \boldsymbol{v}^m, \quad i = 1, \ldots, N. \tag{20}$$

Note that any two POD modes are mutually orthonormal, i.e., $(\boldsymbol{u}_i, \boldsymbol{u}_j)_\Omega = \delta_{ij}$, $\forall i, j \in \{1, \ldots, M\}$. The POD mode amplitudes can be expressed by

$$a_i^m := \sqrt{\lambda_i M} e_m^i, \quad i = 1, \ldots, N. \tag{21}$$

Finally, the POD method decomposes each snapshot into a linear combination of the time coefficients $a_i(t)$ and spatial modes $\boldsymbol{u}_i$,

$$\boldsymbol{u}(\boldsymbol{x}, t) = \boldsymbol{u}_m(\boldsymbol{x}) + \sum_{i=1}^{N} a_i(t)\boldsymbol{u}_i(\boldsymbol{x}), \tag{22}$$

where $N = M - 1$ means the lossless POD decomposition.

Cluster analysis identifies the flow pattern via the similarity metric between any two snapshots. The similarity is measured by the Euclidean distance, expressed by

$$d(\boldsymbol{u}^m, \boldsymbol{u}^n) = \sqrt{\int_\Omega \mathrm{d}x \|\boldsymbol{u}^m - \boldsymbol{u}^n\|^2}. \tag{23}$$

In this equation, the whole computational domain Ω is used for the integration. In the cluster algorithm, many repetitions are required to gain a better result, which leads to extremely expensive calculation. Note that any two POD modes are mutually orthonormal. The distance between any two velocity fields can be converted into the distance of the corresponding POD mode amplitudes, given as

$$d(\boldsymbol{u}^m, \boldsymbol{u}^n) = \|\boldsymbol{u}^m - \boldsymbol{u}^n\|_\Omega = \|\boldsymbol{a}^m - \boldsymbol{a}^n\|. \tag{24}$$

In this way, a large amount of the area/volume integrals in the computation of Euclidean distance for cluster analysis are avoided since the most expensive process has been finished by computing the two-point correlation matrix $\boldsymbol{C}$ 18 in the POD method. Therefore, each snapshot is represented by a time coefficient vector $\boldsymbol{a}^m = [a_1(t_m), a_2(t_m), \ldots, a_{M-1}(t_m)]$. The dataset of velocity snapshots is converted into a large matrix $\boldsymbol{A}$ containing a series of POD time coefficient vectors,

$$\boldsymbol{A} = \begin{pmatrix} a_1(t_1) & \cdots & a_{M-1}(t_1) \\ \vdots & \vdots & \vdots \\ a_1(t_M) & \cdots & a_{M-1}(t_M) \end{pmatrix}. \tag{25}$$

The subsequent clustering and analysis in this paper are conducted based on this matrix. In Sec. III B 2, the cluster analysis algorithm is described based on the POD time coefficients.

2. Clustering analysis to identify characteristic flow patterns

The cluster analysis is a dimension reduction tool that discretizes the high-dimensional state space in an unsupervised manner. To be specific, it partitions the observations/snapshots that are mutually similar to K relatively homogeneous clusters. The homogeneity of each cluster is quantified by the cluster diameter D_k. The representative state of each cluster is described by the centroid $\boldsymbol{c}_k, k = 1, \ldots, K$. The similarity of any two velocity fields $\boldsymbol{u}^m$ and $\boldsymbol{u}^n$ is measured using Euclidean distance D. As mentioned in Eq. (24), the distance of two velocity snapshots $\boldsymbol{u}^m$ and $\boldsymbol{u}^n$ based on the norm associated with the Hilbert space $\mathscr{L}^2(\Omega)$ of square-integrable functions is converted to the distance between two corresponding POD time coefficients $\boldsymbol{a}^m$ and $\boldsymbol{a}^n$. Therefore, the cluster analysis is applied to a sequence of POD time coefficients $\boldsymbol{a}^m = \boldsymbol{a}^m(t^m), m = 1, \ldots, M$. In this study, cluster analysis is achieved using the unsupervised k-means++ algorithm[66] that minimizes the inner-cluster variance and maximizes the inter-cluster variance.

In the k-means++ algorithm, a set of centroids $\boldsymbol{c}_k$ is randomly initialized and their performance can be evaluated by the total inner-cluster variance J of snapshots $\boldsymbol{a}^m$ with respect to their corresponding centroids,

$$J(\boldsymbol{c}_1, \ldots, \boldsymbol{c}_k) = \sum_{k=1}^{K} \sum_{\boldsymbol{a}^m \in \mathscr{C}_k} d(\boldsymbol{a}^m, \boldsymbol{c}_k). \tag{26}$$

The k-means++ algorithm solves this optimization problem through iterations to pursue the minimum inner-cluster variance. The iterations will stop until the convergence is reached, and meanwhile, a set of optimal centroids $\boldsymbol{c}_k^{opt,a} (k = 1, \ldots, K)$ associated with the POD time coefficients are determined,

$$\left(\boldsymbol{c}_1^{opt,a}, \ldots, \boldsymbol{c}_K^{opt,a}\right) = \underset{\boldsymbol{c}_1,\ldots,\boldsymbol{c}_K}{argmin}\, V\left(\boldsymbol{c}_1^a, \ldots, \boldsymbol{c}_K^a\right). \tag{27}$$

The cluster analysis assigns a cluster index to each snapshot that corresponds to the nearest centroid, resulting in the cluster affiliation function,

$$k(\boldsymbol{a}^m) = \arg\min_i \|\boldsymbol{a}^m - \boldsymbol{c}_i^a\|. \tag{28}$$

This function defines K cluster regions as Voronoi cells $\mathscr{C}_k$ surrounding centroids. In order to communicate with other following variables conveniently, a characteristic function is proposed as an alternative of Eq. (28) and reads

$$T_k^m := \begin{cases} 1 & \text{if } \boldsymbol{a}^m \in \mathscr{C}_k, \\ 0 & \text{otherwise}. \end{cases} \tag{29}$$

The centroid is defined as the mean flow of all snapshots belonging to a cluster,

$$\boldsymbol{c}_k = \frac{1}{n_k} \sum_{\boldsymbol{a}^m \in \mathscr{C}_k} \boldsymbol{a}^m = \frac{1}{n_k} \sum_{m=1}^{M} T_k^m \boldsymbol{a}^m, \tag{30}$$

where n_k is the number of snapshots in cluster $\mathscr{C}_k$ and reads

$$n_k = \sum_{m=1}^{M} T_k^m. \tag{31}$$

3. Data postprocessing after cluster analysis

To visualize the centroids, the flow structures are reconstructed via the inverse process of the POD by computing the linear combination of the POD coefficient vector of centroid $\boldsymbol{a}_{i,k}^c$ and POD modes $\boldsymbol{u}_i$, i.e.,

$$\boldsymbol{c}_k(\boldsymbol{x}) = \boldsymbol{u}_m(\boldsymbol{x}) + \sum_{i=1}^{N} a_{i,k}^c \boldsymbol{u}_i(\boldsymbol{x}). \tag{32}$$

Similar to POD and DMD, the transverse fluctuation velocity v' is visualized to show the flow patterns rather than including the mean flow.

The performance of cluster analysis is evaluated by the degree of homogeneity of the resolved subspaces. The diameter of a cluster is the distance between the cluster's two most distant observations. The cluster diameter is the maximum Euclidean distance [see Eq. (23)] between any two velocity fields $\boldsymbol{a}^m$ and $\boldsymbol{a}^n$ within a cluster, and it is expressed as

$$D_k = \max_{m,n}\left(D_{mn} : \boldsymbol{a}^m, \boldsymbol{a}^n \in \mathscr{C}_k\right). \tag{33}$$

The standard deviation is a measure of how closely data are clustered around the mean. Basically, low standard deviation means that data are clustered around the mean, whereas a high standard deviation indicates dispersed data. The standard deviation is defined as

$$R_k = \sqrt{\frac{1}{n_k}\sum_{\boldsymbol{a}^m \in \mathscr{C}_k} \|\boldsymbol{a}^m - \boldsymbol{a}_k^c\|^2}. \tag{34}$$

The dissimilarity between any two representative states can be quantified by the Euclidean distance between their two corresponding centroids in the steady domain Ω. This leads to a $K \times K$ symmetric distance matrix $\boldsymbol{d}$. Each entry d_{ij} of this matrix is defined as

$$d_{ij} = d(\boldsymbol{c}_i, \boldsymbol{c}_j) = \sqrt{\int_\Omega \mathrm{d}x \|\boldsymbol{c}_i - \boldsymbol{c}_j\|^2}. \tag{35}$$

The clusters resolve the regions of the dynamical trajectory associated with various turbulent kinetic energies (TKEs). Herein, we estimate the mean TKE of each cluster using the snapshots in this section,

$$TKE_k = \frac{\sum_{m=1}^{M} T_k^m \|\boldsymbol{a}^m - \overline{\boldsymbol{a}}\|^2}{2\sum_{m=1}^{M} T_k^m}. \tag{36}$$

The probabilistic representation of a dynamical system is defined as

$$q_k := \frac{n_k}{M} = \frac{1}{M}\sum_{m=1}^{M} T_k^m. \tag{37}$$

A probability q_k is approximated in this equation by the ratio of snapshots in cluster k to the total snapshots M. This parameter contains data about the cluster population.

C. Network model for state transitions

In Sec. III B 2, the k-means++ algorithm assigns a cluster index to each snapshot from the training dataset, which leads to a discrete-time cluster affiliation function $k(\boldsymbol{a}^m)$. From a probabilistic standpoint, the link between any two clusters is described using a derived network model. The cluster affiliation function is used to infer the direct transition matrix $\boldsymbol{Q}$ and its related time scale matrix $\boldsymbol{T}$ in the network. The network model, unlike the cluster-based Markov model,[48,51] ignores inner-cluster residency and only considers inter-cluster switches. The element of Q_{ij} and T_{ij} describes an event in which the cluster j takes time T_{ij} to transit to cluster i with the probability Q_{ij}. The direct transition probability Q_{ij} is inferred from the training data as

$$Q_{ij} = \frac{n_{ij}}{n_j}, i, j = 1, \ldots, K, \tag{38}$$

where n_{ij} is the number of transitions from $\mathscr{C}_j$ to $\mathscr{C}_i$ and n_j is the number of transitions departing from $\mathscr{C}_j$ regardless of the terminal points. Note that the key diagonals of the matrix $\boldsymbol{T}$ are all 0 as the lingering in the same cluster is omitted.

A time-delay gained from the training data is embedded into the low-dimensional dynamical system, in contrast to the constant time step of the cluster-based Markov model.[48,51] Assume t_n (t_{n+1}) is the time of the first (last) snapshot to enter (leave) the cluster $\mathscr{C}_i$. The residence time in cluster $\mathscr{C}_i$ is computed using the following formula:

$$\tau_i = t_{n+1} - t_n. \tag{39}$$

The spatial mode in the low-dimensional dynamical system is represented by the centroid $\boldsymbol{c}_i$, which represents the spatial mode in the low-dimensional dynamical system, supposes to stay at the center of this time range $(t_n + t_{n+1})/2$. The individual transition time from cluster j to cluster i is then defined as half the residence time of both clusters and reads

$$\tau_{ij} = \frac{\tau_i + \tau_j}{2} = \frac{t_{n+2} - t_n}{2}. \tag{40}$$

Because of the dynamical system's complexity, the transition trajectory between two clusters may change, resulting in distinct time scales. To characterize time scale, we average the transition durations between clusters, imitating the definition of a centroid, which is the mean of all snapshots belonging to this cluster. The entry of the averaged transition time matrix reads

$$T_{ij} = \langle \tau_{ij} \rangle. \tag{41}$$

The cluster-based network model can also predict the future evolution of a dynamical system with a predetermined initial state. The validation of the model is of significance to gain accurate performance. We do not introduce the detailed algorithm in this paper to focus on the physical understanding of the supersonic mixing layer. Readers are referred to Ref. 54 for the details.

IV. RESULTS AND DISCUSSION

In this section, the TN and TK cases are simulated using the large eddy simulation. The dynamics is thoroughly investigated by comparing CNM output for both TN and TK cases. Section IV A provides an overview of the flow characteristics in order to gain a fundamental understanding. The supersonic mixing layer is characterized by a large range of time and spatial scales, intrinsic high dimensionality, and nonlinear dynamics. Section IV B presents the clustering-derived representative spatial modes (i.e., centroids). Cluster analysis is an entirely data-driven dimension reduction technique for identifying flow patterns. The supersonic mixing layer's high-dimensional state space is projected into $K = 10$ centroids. In Sec. IV C, the cluster-based network model is used to reproduce the high-dimensional nonlinear complex dynamical system of the supersonic mixing layer. To comprehend the dynamics, the state temporal transitions are thoroughly analyzed.

A. Flow features

Numerous publications attest to the significance of the role of the splitter plate in the development of the supersonic mixing layer. The fundamental flow characteristics of the blunt-base supersonic mixing layer are visualized in Fig. 5 using the numerical schlieren

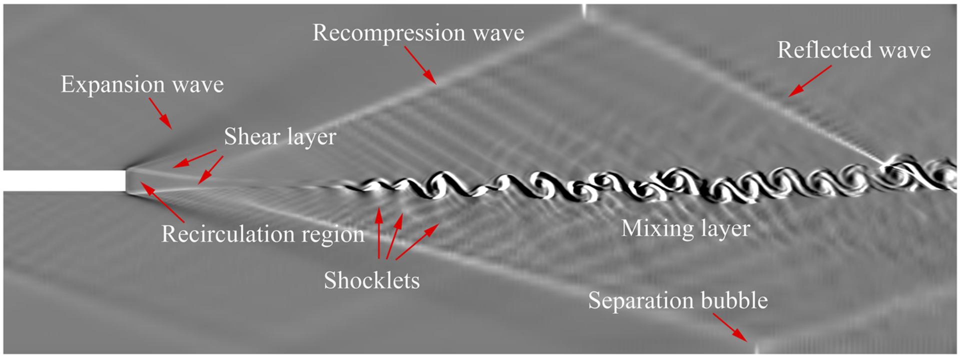

FIG. 5. The fundamental features of the supersonic mixing layer visualized via numerical schlieren[67] in the TK case.

method.[67] This sketch clearly illustrates the layout of wake-mixing layer and shock-mixing layer interactions, which differs from the layout observed in the majority of simulations using a tanh-type velocity profile. Along with the expansion waves, the supersonic streams begin to separate at the trailing edge of the splitter plate. Instead of the immediate confrontation, two streams are separated at the rear of the splitter plate by a low-speed wake. When two shear layers approach the splitter plate's centerline, compression occurs as the flow attempts to realign with the streamwise direction. The compression waves originated in the shear layer's supersonic regions gradually coalesce into the recompression oblique shock wave. Their reflected waves from the upper or lower wall interact with the redeveloping mixing layer and exert influence on the growth process via the modification of compressibility effects along the streamwise direction. Following the disappearance of the wake, the two mainstreams merge into a redeveloping mixing layer. As illustrated in Fig. 5, roll-up typical structures, i.e., K–H vortices, develop downstream of the flow field due to the free mixing layer's inherent K–H instability. We assume that the wake instability has a significant effect on the expansion of the mixing layer, which will be analyzed in Sec. IV B. Maintaining K–H instability results in the pairing and merging process of adjacent vortices, which leads to the growth of the mixing layer. The curvature shocklets are captured astonishingly well in the vicinity of the large-scale structures in Fig. 5.

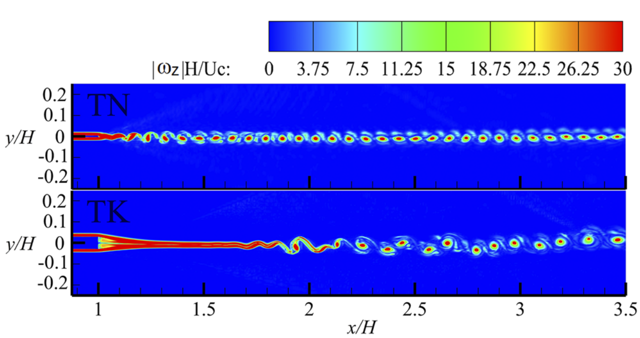

FIG. 6. Instantaneous vorticity contour for the two cases.

The instantaneous vorticity fields for these two cases are compared in Fig. 6 to demonstrate the dynamic difference. Considering the intermittent dynamics of the wake-mixing layer, these two instantaneous images can only provide a primary understanding of flow features. These two examples demonstrate significant differences in wake size, vortex shedding position, and vortex size. As for the TN case, the wake-mixing layer exhibits a rapid roll-up of K–H vortices following a small wake. This indicates that the wake has a negligible effect on the mixing layer dynamics. In comparison, the shedding positions in the TK case are significantly delayed downstream, but larger-scale structures emerge at the start of the redeveloping mixing layer. Note that the occurrence position of shedding is not fixed and generally shows intermittent dynamics. This is further confirmed in the centroids captured in Sec. IV B by the cluster analysis.

B. Spatial modes: Characteristic flow states

To implement the cluster analysis, $M = 2000$ post-transient velocity snapshots are collected with an instant time step of $\Delta\tau = 5\Delta t = 2.5 \times 10^{-7}$ s. The sampling frequency $1/\Delta\tau$ is sufficiently small to capture the relevant dynamics, and the time range of $M = 2000$ snapshots is satisfactory for the accurate statistics. The optimal number of clusters K is a trade-off between the resolution of dynamics and modeling time horizon. These snapshots are first compressed using the POD method to withstand the computational loads generated by the k-means++ algorithm's iterations. These snapshots, denoted by POD time coefficient vectors, are partitioned into $K = 10$ clusters in this paper. The number of clusters $K = 10$ is confirmed to be reasonable for the current dataset, consistent with our previous publications in Refs. 7, 51, and 54. We remark on the critical nature of model validation for the sake of model accuracy. The validation of the CNM via the correlation function is omitted here in order to focus on the mechanism understanding and also for the writing conciseness. Readers are referred to Refs. 7, 51, and 54 for more details.

The homogeneity of each cluster is quantified using the cluster diameter D_k and standard deviation R_k, as shown in Fig. 7. Similar diameter and standard deviation distributions in a case demonstrate the k-means++ algorithm's superior performance, as each cluster is relatively homogeneous in size. The $M = 2000$ snapshots are

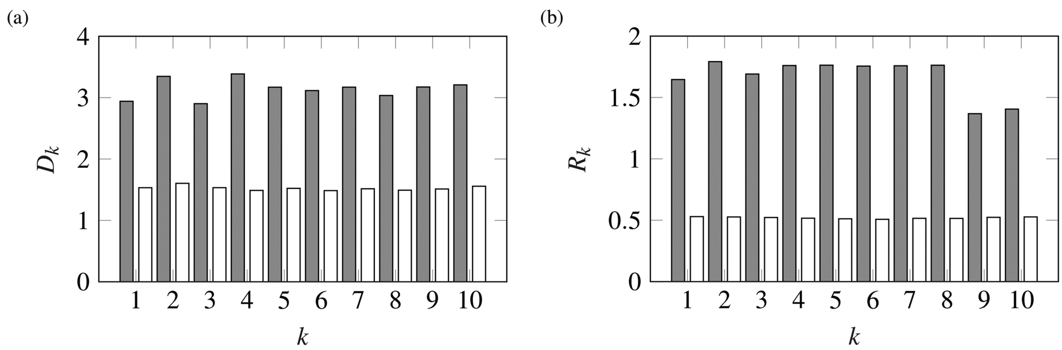

FIG. 7. Cluster diameter D_k (a) and standard deviation R_k (b) of $K = 10$ clusters for TK (gray) and TN (white).

sufficient to fill the high-dimensional state space of the supersonic mixing layer. The clustering process discretizes high-dimensional state space into a set of K subspaces. Clustering projects the high-dimensional state space into K-dimensional subspace. The diameter quantifies the size of a subspace and standard deviations describe the distributed density of observations (snapshots) surrounding the corresponding centroids. Each cluster's D_k and R_k are nearly identical in the TN case, indicating a relatively homogeneous partition of the high-dimensional state space and also implying periodic dynamics. Almost all diameters of TK are more than twice as large as those of the TN cases. The standard deviations of TK (at least $k = 1, \ldots, 8$) are over three times larger than that of the TK case. This implies that, abstractly speaking, the TK case spans a significantly larger state space than the TN case with dispersedly distributed snapshots.

The $K = 10$ centroids can be used to illustrate the representative flow patterns of clusters, as shown in Figs. 8 and 9. Centroids are

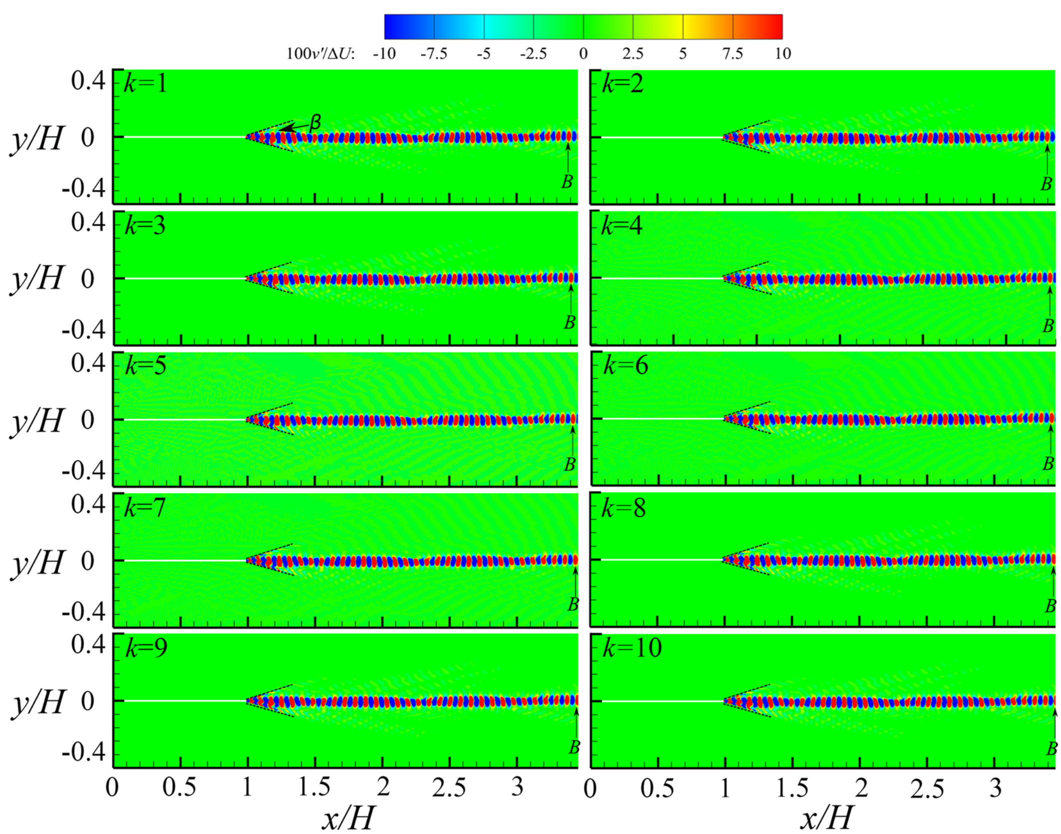

FIG. 8. $K = 10$ centroids in the whole computational domain for the TN case. Only the transverse fluctuation velocity v' is visualized.

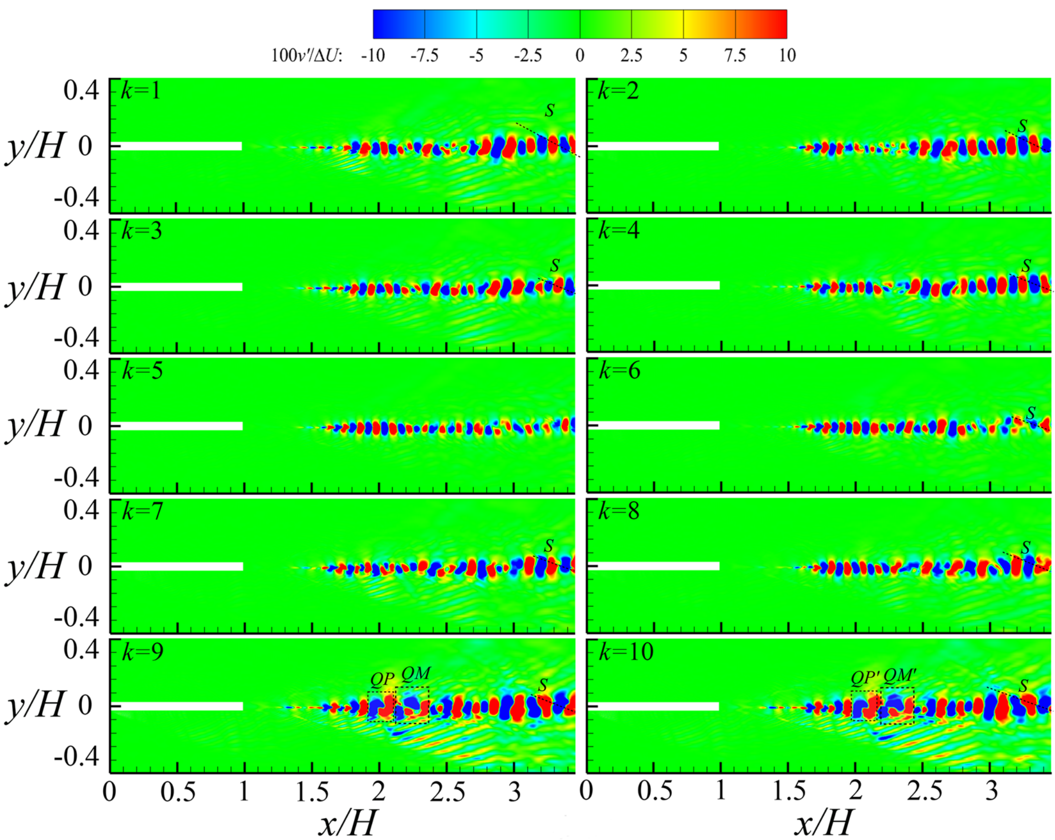

FIG. 9. $K = 10$ centroids in the whole computational domain for the TK case. Only the transverse fluctuation velocity v' is visualized.

reconstructed using the POD method's reverse process, as described in Eq. (32). Each centroid has two components in this study: streamwise velocity and transverse velocity. We visualize the transverse fluctuation velocity v' in this section as it is critical for mass mixing and approaches the vortex structures. We will refer to the transverse fluctuation velocity v' as centroids in the following. These two cases exhibit radically different flow characteristics. In the TN case, the redeveloping mixing layer forms immediately after the trailing edge of the splitter plate. The wake is small enough that its effect on the development of the mixing layer can be completely ignored. This results in a significantly greater advance of the reattachment point in the TN case than in the TK case as illustrated in Fig. 5. The expansion angle β between the upper and lower expansion waves, as shown in Fig. 8, is pretty small. The spatial structure in the TN case is approximately uniform structures in the streamwise direction. Starting at $x/H = 1$, the area occupied by the vortex structures is amplified and gradually decreases until $x/H = 1.5$. Another similar process occurs between $x/H = 1.5$ and $x/H = 2.25$ and also between $x/H = 2.25$ and $x/H = 3$.

Increasing the thickness of the splitter plate greatly affects the spatial and temporal dynamics of the supersonic mixing layer. The TK case contains a variety of structures of varying sizes and shapes. The wake behind the trailing edge has a very low transverse fluctuation velocity v' where the streamwise motions dominate the dynamics of this region. The shapes of the $K = 10$ centroids reveal two distinct subsets: Kelvin–Helmholtz vortices (K–H $k = 1 \ldots 8$) and vortex pairing (VP, $k = 9, 10$). It is widely acknowledged that the VP behavior significantly generates more energy than K–H behavior. In the K–H subset, the wake effects cease to exist at around $x/H = 1.5$, followed by the fast expansion of the mixing area to approximately $x/H = 2$ with the peak. Similarly, after the peak, the mixing area decreases to around $x/H = 2.5$. Subsequently, another increase begins. Various flow behaviors, such as vortex pairing, merging, and tearing, are well captured in the VP subset. In addition, rare events, such as quadruple-vortex pairing/merging, are also clearly resolved in centroids $k = 9, 10$, as denoted by "QP" and "QM" (QP' and QM'). Due to the wide value range of the legend, the wake flow near the trailing edge of the splitter plate is deliberately eliminated in Fig. 9. This area has been magnified to show the fine flow structures of the wake, as illustrated in Fig. 10. The absolute v' amplitudes are only equal to 1 as the maximum ΔU approaches 100. The reattachment points in these centroids are not fixed, which are related to the redeveloping mixing layer's diverse behaviors. The shock-wave/mixing layer interactions are well captured in the majority of centroids, denoted by "S" in Fig. 9. In comparison to the VP subset, the reattachment points of the K–H subset are generally delayed, except for centroid $k = 1$. The unstable position of the reattachment point strengthens the initial turbulence of the

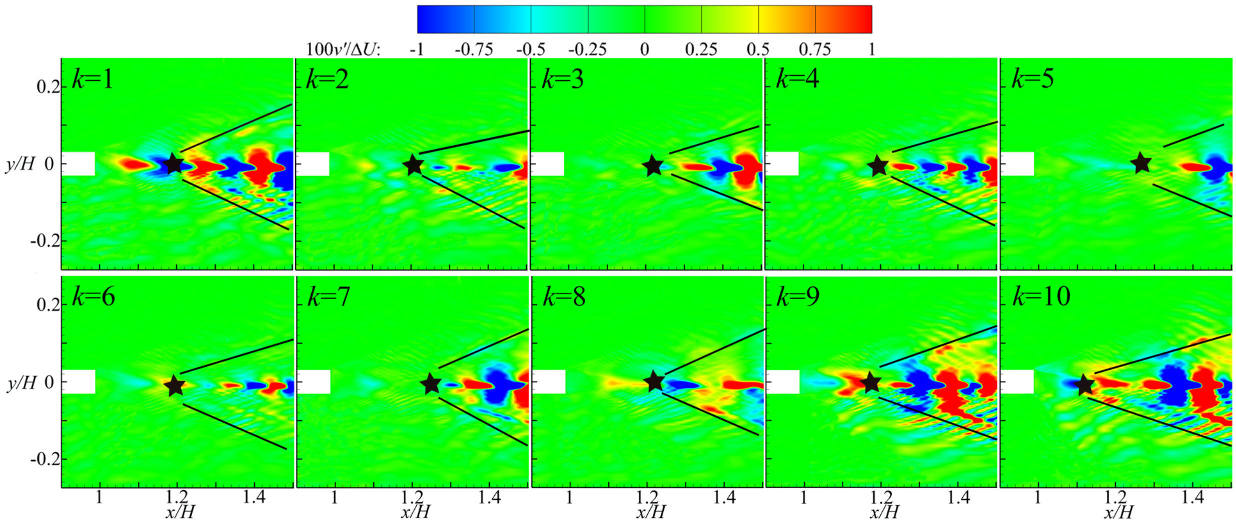

FIG. 10. $K = 10$ centroids near the trailing edge of the splitter plate for the TK case. Only the transverse fluctuation velocity v' is visualized. These figures corresponds to Fig. 9 with a new legend. The star symbol ($\star$) and solid lines denote the reattachment points and reattachment shock waves, respectively. The intersection location of two shock waves approximates the reattachment point. We emphasize that the denoted positions are roughly determined according to the visualization.

redeveloping mixing layer, implying the presence of a variety of dynamical behaviors downstream.

The geometrical difference of the flow structures in the same regime can be overall measured using the Euclidean distance $d(\boldsymbol{c}_i, \boldsymbol{c}_j)$, which results in the symmetry distance matrix $D \in R^{10\times 10}$ [see Eq. (35)]. Figure 11 depicts the symmetrical distance matrix $\boldsymbol{D}$ for TN and TK, respectively. The cluster distance matrix can be used to estimate the trajectory length for cluster transitions as well as the geometric relationship between the centroids. The TN's distance matrix reveals the close association of two adjacent centroids, for example, centroid $\boldsymbol{c}_n$ is mutually similar to centroid $\boldsymbol{c}_{n+1}$. This indeed implies that the flow structures in the convective process move in a periodic manner. The adjacent centroids exhibit a small phase difference almost entirely independent of structure shape modification. The TK's distance matrix is more informative than the TN's since it further highlights the difference between two regimes as mentioned above: the K–H and VP.

C. Dynamics analysis: State temporal transitions

The CNM extracts a sequence of events from a probabilistic point of view, providing an in-depth insight into the flow dynamics of the supersonic mixing layer, especially the intermittent behavior. After cluster analysis, the k-means algorithm assigns an affiliation

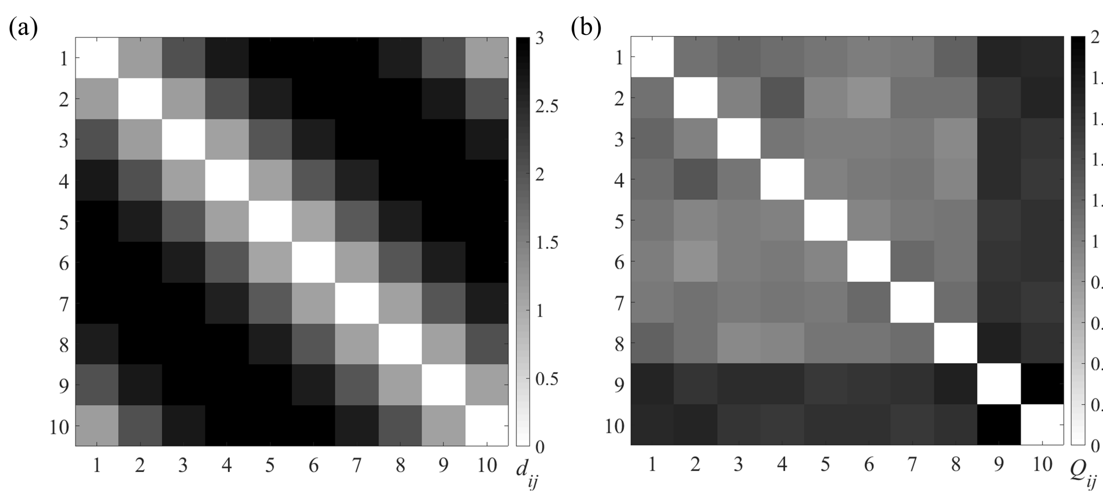

FIG. 11. Cluster distance matrix $\boldsymbol{D}$ [see Eq. (35)]. (a) TN and (b) TK. Distances are linearly scaled with all zero elements in the diagonal.

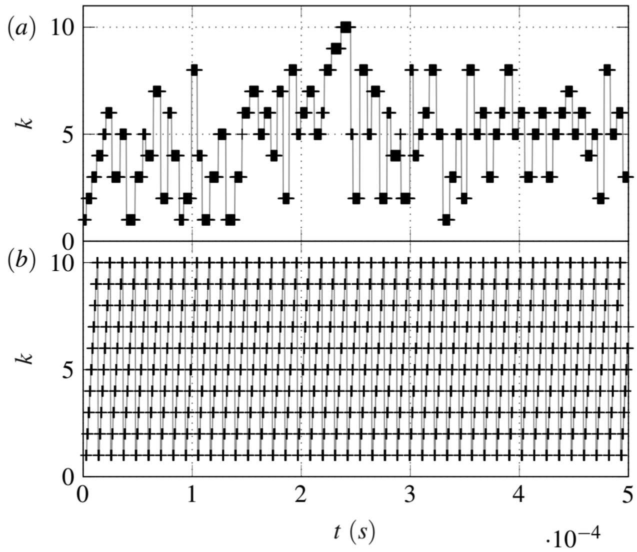

FIG. 12. Cluster affiliation function (a) TK and (b) TN.

to each snapshot, which is the index of the corresponding nearest centroid of the snapshot. As illustrated in Fig. 12, the cluster affiliation function depicts the cluster temporal transition among training data, i.e., these $M = 2000$ snapshots. We establish a rule that the first cluster to appear is designated cluster $k = 1$. Then, the subsequent newly appearing cluster is considered to be $k + 1$. These cluster transitions are summarized using a direct transition matrix (DTM) $\boldsymbol{Q}$ with the averaged time scale, i.e., averaged transition time matrix $\boldsymbol{T}$, as shown in Figs. 13 and 14, respectively. The TN case exhibits strictly periodic dynamics with a cycled state visit at centroid $1 \rightarrow 2, \ldots, 9 \rightarrow 10$. As shown in Fig. 16, there is no fluctuation for the turbulent kinetic energy during the periodic dynamics, which indicates the same contributions of each cluster to the flow mixing. The resolved centroids move downstream continuously with a short distance between adjacent centroids. As shown in Fig. 8, a vortex denoted as "B" convects downstream from centroid $k = 1$ until this structure propagates out of the computational domain in centroid $k = 10$. The vortex's geometrical modification is almost unheeded except the phase difference in this cycled behavior. In addition, the expansion angle denoted by "β" in Fig. 8 formed by the two expansion waves is not changed in the periodic motion. The observations belonging to each cluster are equally distributed in population with a probability $q_k^{TN} \approx 0.1, k = 1, \ldots, 10$, as shown by white rectangles in Fig. 15.

We must emphasize that the TN case displays pretty special dynamics only with K–H vortices in the community of the supersonic mixing layer. The disappearance of the vortex pairing could result from the limited length of the computational domain. In addition, the length of the splitter plate L_s, inflow conditions of the numerical simulation, and Reynolds number could also significantly affect the dynamics. We focus on the dynamics of the given supersonic mixing layer instead of discussing these factors.

Increasing the thickness of the splitter plate entangles the flow dynamics of the TK case with a highly random and chaotic state. As shown in Fig. 16, the energy of all TK's clusters is much higher than that of TN. However, the population exhibits maldistribution, which is assembled in the first several clusters. The VP regime $k = 9, 10$ with larger TKE is populated at a pretty small probability. The K–H subset contains the majority of state transitions among TK's clusters, which are accompanied by a small fluctuation in turbulent kinetic energy (see Fig. 16). The phenomenon is explained by the probability distribution q_k, which shows that the K–H clusters are overall populated at 96.45%. The direct transition matrix $\boldsymbol{Q}$ can be used to investigate the dynamics of state transitions. The cluster $k = 1$ is assumed to be the initial state as this cluster is populated at the largest probability. In the dynamics, only the most probabilistic transition route is considered. The cluster $k = 1$ prefers cluster $k = 3$ as the next state. Then, within the K–H regime, there is one cyclic motion with high

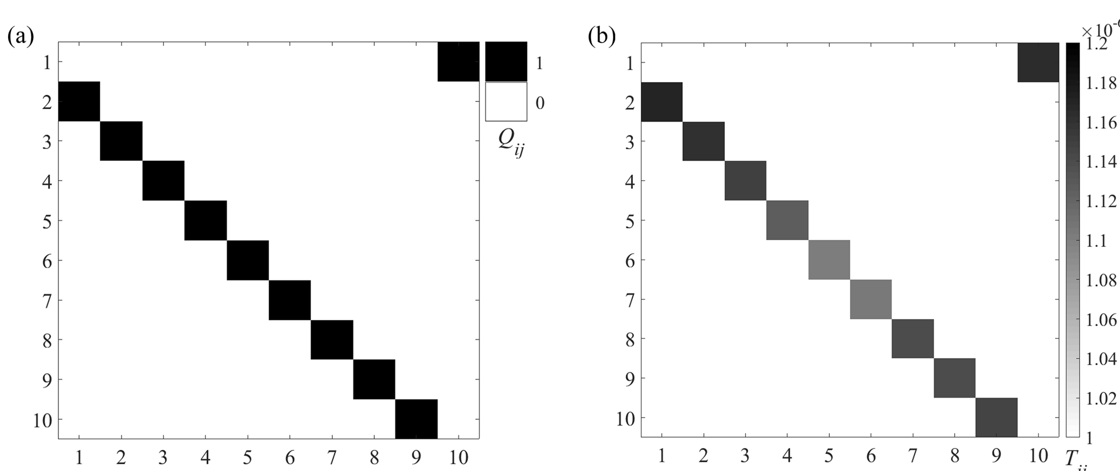

FIG. 13. Cluster-based network model for TN case. (a) Direct transition matrix $\boldsymbol{Q}$. (b) Averaged transition time matrix $\boldsymbol{T}$. $\boldsymbol{Q}$ and $\boldsymbol{T}$ have the same geometry. White areas in two figures denote the zero elements. All elements of $\boldsymbol{Q}$ are 1.

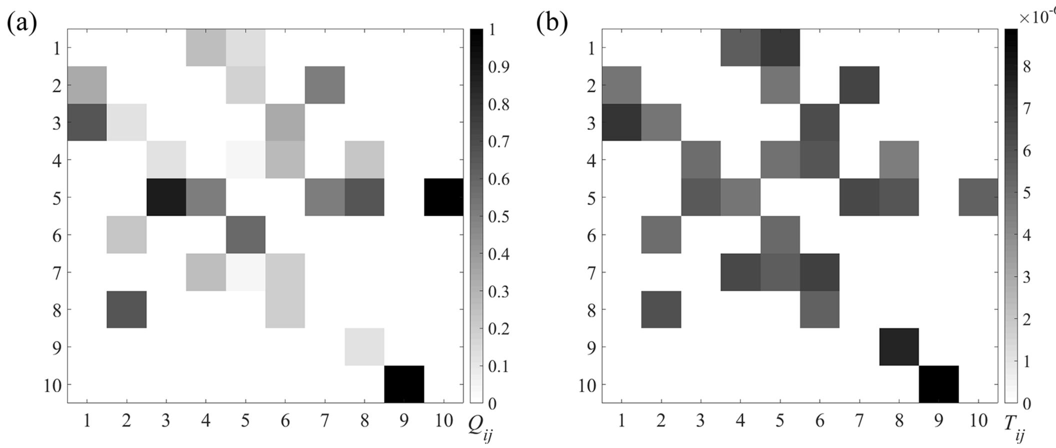

FIG. 14. Cluster-based network model for the TK case. (a) Direct transition matrix $\boldsymbol{Q}$. (b) Averaged transition time matrix $\boldsymbol{T}$.

probability: 3 → 5 → 6 → 3. The flow starts with an advanced reattachment point (denoted by a ⋆ in Fig. 10), revealing fast development of the mixing layer of dual mainstreams at around $x/H = 1.24$ in cluster $k = 1$ (see Fig. 10). We emphasize that the reattachment point and reattachment shock are determined roughly according to the visualization instead of the accurate detection method. The numerical schlieren[67,68] could be a good choice. This state takes longer to transit into the cluster $k = 3$ [see Fig. 14(b)], where the reattachment point and redeveloping mixing layer are both delayed to around $x/H = 1.30$. The expansion angle is also found to decrease. The cluster $k = 5$ follows the trend of the two characteristic flow features being further postponed to $x/H = 1.38$ and then advanced to $x/H = 1.3$ in cluster $k = 3$. During the intermittent evolution, the size of the wake oscillates in a similar way. In contrast to the loop motions in the TN case, the wake effects on the downstream mixing layer are greatly amplified, affecting the downstream redeveloping mixing layer. The advanced (delayed) reattachment point, as shown in Figs. 9 and 10, indicates the complicated (simple) vortex structures in the near field but simple (complicated) vortex structures in the far field. The turbulent kinetic energy carried by each cluster in the cyclic motion is remarkably similar, with only minor variations. Beginning with cluster $k = 1$, the carried turbulent kinetic energy gradually climbs to the peak with cluster $k = 5$. In the near field, the centroid $\boldsymbol{c}_5$ exhibits a fast expansion of the K–H vortex, while in the far field, vortex pairing/merging and vortex tearing can be observed.

With a smaller probability, the cluster $k = 1$ could select the cluster $k = 2$ as the next state. Then, the following transition is → 8 → 5 → 6 → 3. The cluster $k = 2$ passes through cluster $k = 8$ to enter the route the same as that with the highest probability. The reattachment point displays a slower downstream motion in the cyclic motion. Meanwhile, the TKE fluctuation exhibits a similar trend that climbs into the peak at cluster $k = 5$ and then decreases. In these two dynamical routes, the cluster $k = 5$ is the only node that must be passed. The cluster $k = 3$ serves as the terminal state. In the K–H regime, a delayed reattachment point reveals more complicated structures in the far field with the larger TKE.

The cluster $k = 5$ acts as a bifurcation point in both dynamical routes. Apart from returning to cluster $k = 3$ via cluster $k = 6$, the cluster $k = 5$ has four additional evolutions, including a direct

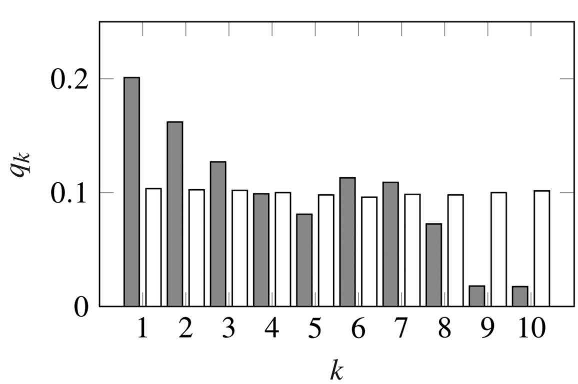

FIG. 15. Cluster population probability q_k for the TK (gray) and TN (white) case.

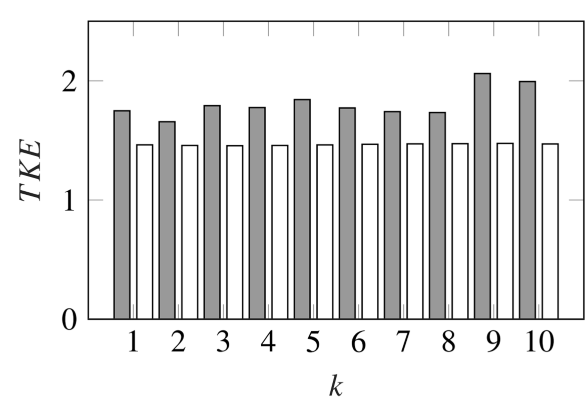

FIG. 16. The turbulent kinetic energy of each cluster for the TK (gray) and TN (white).

return to cluster $k = 1$ forming a closed-loop, passing through cluster $k = 4$ with a lower probability, transiting to cluster $k = 2$ followed by a new evolution, and immediately transiting to cluster $k = 7$. Throughout these evolutions, the reattachment point oscillates forward and downward in response to the TKE fluctuation and the stretching of the flow structures. The VP regime $k = 9, 10$ can be merely accessed by the cluster $k = 8$ and then reverted to the K–H regime via cluster $k = 5$. The VP regime only accounts for a negligible portion with 3.55%, as shown in Fig. 15. This implies that the VP remains a rare event in the supersonic mixing layer with a 5 mm splitter plate despite the fact that the individual centroid of the VP regime contains more turbulent kinetic energy than the K–H regime, as shown in Fig. 16. This indicates that the K–H regime is found difficult to reach a high-energy level. The state transition from cluster $k = 9$ to cluster $k = 10$ is unidirectional in the VP subset. The flow structures retain their original shapes during this evolution, as illustrated in in Fig. 9. With rotational deformation, the QP and QM structures migrate downstream evolve into QP' and QM'. To quantify the overall energy fluctuation in a particular dynamical system, we define the weight-average cluster TKE as the overall captured energy $\overline{E} = \sum_{k=1}^{K} q_k TKE_k$. In the TK case, the overall fluctuation energy ($\overline{E} = 1.76$) is 20.5% larger than that of the TN case ($\overline{E} = 1.46$).

V. CONCLUSION

In this article, the flow dynamics of a blunt base supersonic mixing layer is analyzed using the cluster-based network model (CNM). The mechanism of the wake/mixing layer attractor is comprehensively understood in comparison to a given benchmark with the eliminated wake effect. With only ten physical centroids, the CNM resolves the dynamical system of the broadband supersonic mixing layer. The direct transition matrix $\boldsymbol{Q}$ and averaged transition time matrix $\boldsymbol{T}$ define the spatial and time scales of the ten-centroid based low-dimensional model, respectively. In the given baseline case, the CNM identifies only one flow pattern existing in the dynamical system: the K–H regime. The given baseline case exhibits strictly periodic transitions between these ten K–H clusters with a nearly constant turbulent kinetic energy. Each cluster is equally populated with a probability $q_k^{TN} \approx 0.1, k = 1, \ldots, 10$. Increasing the thickness of the splitter plate undergoing a wake results in highly complicated flow behaviors from spatial and temporal points of view. In the supersonic blunt base mixing layer, the CNM identifies two distinct flow regimes: K–H and VP. The cluster diameter D_k and standard deviation R_k reveal that the TK case spans significantly larger state space than the TN case. Each cluster of the TK case in the given regime brings much larger TKE than that of the TN case. In contrast to the TN case, the TK case results in vortex pairing/merging and the formation of more complex flow structures. In terms of temporal dynamics, the flow structures exhibit highly intermittent behaviors with small amplitude fluctuation. The CNM has identified some probable routes for state transitions and the related bifurcation point, which aids in the design of control strategy. The control design using the CNM is via changed direct transition probability $\boldsymbol{Q}$ and changed transition time $\boldsymbol{T}$. Appendix C4 in Ref. 54 gives a framework of the flow control strategy.

The present study gives an example to analyze the given blunt base supersonic mixing layer using the CNM. The resolved instantaneous behaviors are described in two-dimensional flow fields as graphical means instead of one-dimensional signals. Additionally, the CNM provides a set of useful methods for quantifying the similarity of representative states, carried energies, mode switching time scales, and metrics in high-dimensional state space. In general, the CNM opens a novel automatable avenue for nonlinear dynamical modeling.

When the splitter plate thickness is small or when the inlet tanh profile is embedded, the dominant instability inclines to be convective in nature. The wake behind the splitter plate's trailing edge behaves global instability, which exacerbates the initial instability of the redeveloping mixing layer. The asymmetric conditions in the upward wake flow further complicate the flow dynamics. However, increasing the thickness from 1 to 5 mm does not significantly magnify the turbulent kinetics. The TKE is only raised by 20.5%, which is much less than the cavity-actuated supersonic mixing layer.[7] In practice, the thickness of the splitter plate is invariably increased and the flow parameters are also temporally changed during engine operation. The comparison of direct transition matrices reveals the dynamical difference in regimes with various initial conditions, i.e., the thickness of the splitter plate in this study. This paper inspires the critical nature of geometrical dimensions for splitter plate while developing a supersonic mixer. There should exist a set of geometrical parameters that are optimal for given incoming flow parameters. Indeed, the CNM provides a means of optimizing the flow system to meet the needs of researchers. This merits further exploration, which the authors intend to do in the future.

ACKNOWLEDGMENTS

H.L. appreciates the National Natural Science Foundation of China (Grant No. 91441121) and Graduate Student Research Innovation Project of Hunan Province (Grant No. CX2018B027). He gratefully acknowledges the support of the China Scholarship Council (CSC) (Grant No. CSC201803170267) during his study in Technische Universität Berlin and the excellent working conditions of the Hermann-Föttinger-Institut. He greatly appreciates the computing sources and technical support provided by the National Supercomputer Center in GuangZhou. We appreciate valuable stimulating discussions with Professor J. G. Tan and Professor Bernd Noack.

The authors declare there is no conflict of interest regarding the publication of this paper.

DATA AVAILABILITY

The data that support the findings of this study are available from the corresponding author upon reasonable request.

REFERENCES

[1] A. V. G. Cavalieri, P. Jordan, Y. Gervais, M. Wei, and J. B. Freund, "Intermittent sound generation and its control in a free-shear flow," Phys. Fluids **22**, 115113 (2010).

[2] D. Casalino, F. Diozzi, R. Sannino, and A. Paonessa, "Aircraft noise reduction technologies: A bibliographic review," Aerosp. Sci. Technol. **12**, 1–17 (2008).

[3] R. Li, B. R. Noack, L. Cordier, J. Borée, and F. Harambat, "Drag reduction of a car model by linear genetic programming control," Exp. Fluids **58**, 103 (2017).

[4] X.-W. Sun, W. Liu, and Z.-X. Chai, "Method of investigation for numerical simulation on aero-optical effect based on WCNS-E-5," AIAA J. **57**(5), 1–13 (2019).

[5]T. C. Island, W. D. Urban, and M. G. Mungal, "Mixing enhancement in compressible shear layers via sub-boundary layer disturbances," Phys. Fluids **10**, 1008–1020 (1998).
[6]H. Li, J. Tan, D. Zhang, and J. Hou, "Investigations on flow and growth properties of a cavity-actuated supersonic planar mixing layer downstream a thick splitter plate," Int. J. Heat Fluid Flow **74**, 209–220 (2018).
[7]J. Tan, H. Li, and B. R. Noack, "On the cavity-actuated supersonic mixing layer downstream a thick splitter plate," Phys. Fluids **32**, 096102 (2020).
[8]A. W. Vreman, N. D. Sandham, and K. H. Luo, "Compressible mixing layer growth rate and turbulence characteristics," J. Fluid Mech. **320**, 235–258 (1996).
[9]B. Jones, "Statistical investigation of pressure and velocity fields in the turbulent two-stream mixing layer," in 4th Fluid and Plasma Dynamics Conference, 1971.
[10]G. L. Brown and A. Roshko, "On density effects and large structure in turbulent mixing layers," J. Fluid Mech. **64**, 775–816 (1974).
[11]P. Ortwerth and A. Shine, "On the scaling of plane turbulent shear layers," Laser Digest, Report No. AFWL-TR-77-118, 1977, p. 115.
[12]P. E. Dimotakis and G. L. Brown, "The mixing layer at high Reynolds number: Large-structure dynamics and entrainment," J. Fluid Mech. **78**, 535–560 (1976).
[13]J. H. Bell and R. D. Mehta, "Development of a two-stream mixing layer from tripped and untripped boundary layers," AIAA J. **28**, 2034–2042 (1990).
[14]S. G. Goebel, J. C. Dutton, H. Krier, and J. P. Renie, "Mean and turbulent velocity measurements of supersonic mixing layers," Miner. Deposita **29**, 263–272 (1994).
[15]S. G. Goebel and J. C. Dutton, "Experimental study of compressible turbulent mixing layers," AIAA J. **29**, 538–546 (1991).
[16]C. Pantano and S. Sarkar, "A study of compressibility effects in the high-speed turbulent shear layer using direct simulation," J. Fluid Mech. **451**, 329–371 (2002).
[17]W. D. Urban and M. G. Mungal, "Planar velocity measurements in compressible mixing layers," J. Fluid Mech. **431**, 189–222 (2001).
[18]M. G. Olsen and J. C. Dutton, "Planar velocity measurements in a weakly compressible mixing layer," J. Fluid Mech. **486**, 51–77 (2003).
[19]D. W. Bogdanoff, "Compressibility effects in turbulent shear layers," AIAA J. **21**, 926–927 (1983).
[20]S. Ghosh and R. Friedrich, "Effects of radiative heat transfer on the turbulence structure in inert and reacting mixing layers," Phys. Fluids **27**, 055107 (2015).
[21]M. Ferrer, P. José, G. Lehnasch, and A. Mura, "Compressibility and heat release effects in high-speed reactive mixing layers I: Growth rates and turbulence characteristics," Combust. Flame **180**, 284–303 (2017).
[22]B. Thurow, M. Samimy, and W. Lempert, "Compressibility effects on turbulence structures of axisymmetric mixing layers," Phys. Fluids **15**, 1755–1765 (2003).
[23]T. Kanda, K. Tani, and K. Kudo, "Conceptual study of a rocket-ramjet combined-cycle engine for an aerospace plane," J. Propul. Power **23**, 301–309 (2007).
[24]Q. Dai, T. Jin, K. Luo, and J. Fan, "Direct numerical simulation of particle dispersion in a three-dimensional spatially developing compressible mixing layer," Phys. Fluids **30**, 113301 (2018).
[25]Q. Dai, T. Jin, K. Luo, and J. Fan, "Direct numerical simulation of a three-dimensional spatially evolving compressible mixing layer laden with particles. I. Turbulent structures and asymmetric properties," Phys. Fluids **31**, 083302 (2019).
[26]D. Chong, Y. Bai, Q. Zhao, W. Chen, J. Yan, and Y. Hong, "Direct numerical simulation of vortex structures during the late stage of the transition process in a compressible mixing layer," Phys. Fluids **33**, 054108 (2021).
[27]T. Matsushima, K. Nagata, and T. Watanabe, "Wavelet analysis of shearless turbulent mixing layer," Phys. Fluids **33**, 025109 (2021).
[28]E. J. Gutmark, K. C. Schadow, and K. H. Yu, "Mixing enhancement in supersonic free shear flows," Annu. Rev. Fluid Mech. **27**, 375–417 (1995).
[29]J. Tan, D. Zhang, and L. Lv, "A review on enhanced mixing methods in supersonic mixing layer flows," Acta Astronaut. **152**, 310–324 (2018).
[30]X.-x. Fang, C.-b. Shen, M.-b. Sun, R. D. Sandberg, and P. Wang, "Flow structures of a lobed mixer and effects of streamwise vortices on mixing enhancement," Phys. Fluids **31**, 066102 (2019).
[31]X.-x. Fang, C.-b. Shen, M.-b. Sun, H.-b. Wang, and P. Wang, "Turbulent structures and mixing enhancement with lobed mixers in a supersonic mixing layer," Phys. Fluids **32**, 041701 (2020).
[32]S. Yadala, N. Benard, M. Kotsonis, and E. Moreau, "Effect of dielectric barrier discharge plasma actuators on vortical structures in a mixing layer," Phys. Fluids **32**, 124111 (2020).
[33]R. D. Mehta, "Effect of velocity ratio on plane mixing layer development: Influence of the splitter plate wake," Exp. Fluids **10**, 194–204 (1991).
[34]N. D. Sandham and R. D. Sandberg, "Direct numerical simulation of the early development of a turbulent mixing layer downstream of a splitter plate," J. Turbul. **10**, N1 (2009).
[35]S. Laizet, S. Lardeau, and E. Lamballais, "Direct numerical simulation of a mixing layer downstream a thick splitter plate," Phys. Fluids **22**, 015104 (2010).
[36]C. Braud, D. Heitz, P. Braud, G. Arroyo, and J. Delville, "Analysis of the wake mixing-layer interaction using multiple plane PIV and 3D classical POD," Exp. Fluids **37**, 95–104 (2004).
[37]M. Rajaee, S. K. F. Karlsson, and L. Sirovich, "Low-dimensional description of free-shear-flow coherent structures and their dynamical behaviour," J. Fluid Mech. **258**, 1–29 (1994).
[38]G. Song, F. Alizard, J.-C. Robinet, and X. Gloerfelt, "Global and Koopman modes analysis of sound generation in mixing layers," Phys. Fluids **25**, 124101 (2013).
[39]R. K. Soni and A. De, "Investigation of mixing characteristics in strut injectors using modal decomposition," Phys. Fluids **30**, 016108 (2018).
[40]P. J. Schmid, "Dynamic mode decomposition of numerical and experimental data," J. Fluid Mech. **656**, 5–28 (2010).
[41]K. Taira, S. L. Brunton, S. T. M. Dawson, C. W. Rowley, T. Colonius, B. J. McKeon, O. T. Schmidt, S. Gordeyev, V. Theofilis, and L. S. Ukeiley, "Modal analysis of fluid flows: An overview," AIAA J. **55**, 4013–4041 (2017).
[42]B. R. Noack, W. Stankiewicz, M. Morzyński, and P. J. Schmid, "Recursive dynamic mode decomposition of transient and post-transient wake flows," J. Fluid Mech. **809**, 843–872 (2016).
[43]S. Le Clainche and J. M. Vega, "Spatio-temporal Koopman decomposition," J. Nonlinear Sci. **28**, 1793–1842 (2018).
[44]S. Le Clainche, J. M. Pérez, and J. M. Vega, "Spatio-temporal flow structures in the three-dimensional wake of a circular cylinder," Fluid Dyn. Res. **50**, 051406 (2018).
[45]K. K. Chen, J. H. Tu, and C. W. Rowley, "Variants of dynamic mode decomposition: Boundary condition, Koopman, and Fourier analyses," J. Nonlinear Sci. **22**, 887–915 (2012).
[46]J. Burkardt, M. Gunzburger, and H.-C. Lee, "Centroidal Voronoi tessellation-based reduced-order modeling of complex systems," SIAM J. Sci. Comput. **28**, 459–484 (2006).
[47]J. Burkardt, M. Gunzburger, and H.-C. Lee, "POD and CVT-based reduced-order modeling of Navier–Stokes flows," Comput. Methods Appl. Mech. Eng. **196**, 337–355 (2006).
[48]E. Kaiser, B. R. Noack, L. Cordier, A. Spohn, M. Segond, M. Abel, G. Daviller, J. Östh, S. Krajnović, R. K. Niven *et al.*, "Cluster-based reduced-order modelling of a mixing layer," J. Fluid Mech. **754**, 365–414 (2014).
[49]J. Östh, E. Kaiser, S. Krajnović, and B. R. Noack, "Cluster-based reduced-order modelling of the flow in the wake of a high speed train," J. Wind Eng. Ind. Aerodyn. **145**, 327–338 (2015).
[50]Z. Wei, Z. Yang, C. Xia, and Q. Li, "Cluster-based reduced-order modeling of the wake stabilization mechanism behind a twisted cylinder," J. Wind Eng. Ind. Aerodyn. **171**, 288–303 (2017).
[51]H. Li and J. Tan, "Cluster-based Markov model to understand the transition dynamics of a supersonic mixing layer," Phys. Fluids **32**, 056104 (2020).
[52]N. Ali, M. Calaf, and R. B. Cal, "Cluster-based probabilistic structure dynamical model of wind turbine wake," J. Turbul. **22**, 497–516 (2021).
[53]A. A. Shahbazi and V. Esfahanian, "Reduced-order modeling of lead-acid battery using cluster analysis and orthogonal cluster analysis method," Int. J. Energy Res. **43**, 6779–6798 (2019).
[54]H. Li, D. Fernex, R. Semaan, J. Tan, M. Morzyński, and B. R. Noack, "Cluster-based network model," J. Fluid Mech. **906**, A21 (2021).
[55]D. Fernex, B. R. Noack, and R. Semaan, "Cluster-based network modeling—From snapshots to complex dynamical systems," Sci. Adv. **7**, eabf5006 (2021).

[56] N. T. Clemens and M. G. Mungal, "Large-scale structure and entrainment in the supersonic mixing layer," J. Fluid Mech. **284**, 171–216 (1995).
[57] H. Li, J.-g. Tan, J.-w. Hou, and D.-d. Zhang, "Investigations of self-excited vibration in splitter plate with a cavity in the supersonic mixing layer," Aerosp. Sci. Technol. **74**, 120–131 (2018).
[58] M. Germano, "Turbulence: The filtering approach," J. Fluid Mech. **238**, 325–336 (1992).
[59] J. Hinze and J. Hinze, *Turbulence*, McGraw-Hill Classic Textbook Reissue Series (McGraw-Hill, 1975).
[60] J. Smagorinsky, "General circulation experiments with the primitive equations: I. The basic experiment," Mon. Weather Rev. **91**, 99–164 (1963).
[61] T. J. Poinsot and S. K. Lelef, "Boundary conditions for direct simulations of compressible viscous flows," J. Comput. Phys. **101**, 104–129 (1992).
[62] K. Taira, A. G. Nair, and S. L. Brunton, "Network structure of two-dimensional decaying isotropic turbulence," J. Fluid Mech. **795**, R2 (2016).
[63] A. Guha and K. Pradhan, "Secondary motion in three-dimensional branching networks," Phys. Fluids **29**, 063602 (2017).
[64] K. Pradhan and A. Guha, "Fluid dynamics of oscillatory flow in three-dimensional branching networks," Phys. Fluids **31**, 063601 (2019).
[65] J. L. Lumley, "The structure of inhomogeneous turbulent flows," in *Atmospheric Turbulence and Radio Wave Propagation* (University of California Press, 1967) pp. 166–177.
[66] J. MacQueen, "Some methods for classification and analysis of multivariate observations," in *Proceedings of the Fifth Berkeley Symposium on Mathematical Statistics and Probability* (University of California Press, 1967), Vol. 1, pp. 281–297.
[67] A. Hadjadj and A. Kudryavtsev, "Computation and flow visualization in high-speed aerodynamics," J. Turbul. **6**(16), 33–81 (2005).
[68] C. M. Stack, R. Bhaskaran, and M. C. Adler, and D. V. Gaitonde "Influence of the splitter plate thickness on the near-wake dynamics of compressible turbulent mixing layers," in AIAA SciTech 2019 Forum, 2019.